



PCCP

Lifetimes and decay mechanisms of isotopically substituted ozone above the dissociation threshold: Matching quantum and classical dynamics

Journal:	<i>Physical Chemistry Chemical Physics</i>
Manuscript ID	CP-ART-09-2023-004286.R1
Article Type:	Paper
Date Submitted by the Author:	08-Dec-2023
Complete List of Authors:	Kokoouline, Viatcheslav; University of Central Florida, Physics Alijah, Alexander; Université de Reims, Groupe de Spectrométrie Moléculaire Tyuterev, Vladimir; Laboratory of Molecular Quantum Mechanics and Radiative transfer, Tomsk State University; Laboratory of Theoretical Spectroscopy, V.E. Zuev Institute of Atmospheric Optics, Russian Academy of Sciences

SCHOLARONE™
Manuscripts

Lifetimes and decay mechanisms of isotopically substituted ozone above the dissociation threshold: Matching quantum and classical dynamics

Viatcheslav Kokoouline¹, Alexander Alijah², and Vladimir Tyuterev^{3,4}

¹*Department of Physics, University of Central Florida, Orlando, FL 32816, USA*

²*Groupe de Spectrométrie Moléculaire et Atmosphérique, UMR CNRS 7331, University of Reims Champagne-Ardenne, F-51687, Reims Cedex 2, France*

³*Laboratory of Molecular Quantum Mechanics and Radiative transfer, Tomsk State University, Tomsk, Russia*

⁴*Laboratory of Theoretical Spectroscopy, V.E. Zuev Institute of Atmospheric Optics, Russian Academy of Sciences, 634055, Tomsk, Russia*

(Dated: December 14, 2023)

Submitted: September 3, 2023

Energies and lifetimes of vibrational resonances were computed for ¹⁸O-enriched isotopologue ⁵⁰O₃ = {¹⁶O¹⁶O¹⁸O and ¹⁶O¹⁸O¹⁶O} of the ozone molecule using hyperspherical coordinates and the method of complex absorbing potential. Various types of the scattering resonances were identified, including roaming OO–O rotational states, the series corresponding to continuation of bound vibrational resonances of highly excited bending or symmetric stretching vibrational modes. Such series become metastable above the dissociation limit. The coupling between the vibrationally excited O₂ fragment and the rotational roaming gives rise to Feshbach type resonances in ozone. Different paths for the formation and decay of symmetric ¹⁶O¹⁸O¹⁶O and asymmetric species ¹⁶O¹⁶O¹⁸O were also identified. The symmetry properties of the total rovibronic wave functions of the ¹⁸O-enriched isotopologues are discussed in the context of allowed dissociation channels.

PACS numbers:

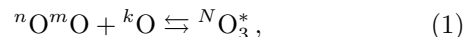
I. INTRODUCTION

The study of isotopic variations has a wide range of applications, from nuclear astrophysics to geochemistry and biochemistry. As an example, such studies can provide an insight into the climate in the past, measuring isotope composition of compounds preserved in ancient terrestrial materials, ice and sediment cores [1–6]. Oxygen is one of the most abundant elements on Earth that has three stable isotopes: ¹⁶O, ¹⁷O and ¹⁸O. The origin and abundance of these isotopes could bring information on nuclear processes in nova and supernova stars [7–12]: Ejected traces of the stars were found in unusual isotopic abundance in several-billion-year-old meteorites [6, 13]. Different isotopes can react at different rates. Usually, isotope effects scale proportionally to relative mass differences, the corresponding mass fractionation laws for the same process but involving different isotopologues are called mass-dependent [14] fractionation (MDF). The isotopic variability of oxygen in the solar system and large mass dependent fractionation on Earth, with a difference between the atmosphere and hydrosphere was the subject of many measurements as recently reviewed by Ireland *et al.* [12]. A higher fraction of the heavy ¹⁸O isotope was reported in the lower atmosphere compared to the ocean water [15]. An isotopic enrichment in the oxygen is consistent with the MDF and was attributed to the biological activity [15, 16]. Oxygen isotopes in single-celled organism sediments provides information on changes in ocean temperatures over the last 70 million years [17]. Recent astrophysical studies suggest that the distribution of oxygen isotopes can help understanding

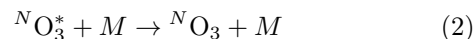
the formation processes of the solar system and other exoplanetary systems [12].

In some cases, the isotopic reaction products show significant difference from the usual MDF laws, they are called mass-independent fractionations (MIF) or, sometimes, non-MDF effects. For details see [4, 6, 18–21] and references therein. This MIF effect is the most pronounced for the isotopic variant of the ozone molecule [22–32]. It has been found in meteorites [13], in laboratory electric discharge experiments [23, 24], and in the upper atmosphere [22, 25–27, 33]. It has puzzled the chemistry community for nearly four decades being considered as a “fascinating and surprising aspect . . . of selective enrichment of heavy ozone isotopomers” [34] and “a well-recognized milestone in the study of isotope effect” [31].

The MIF discovery was a motivation for a large number of experimental and theoretical studies. Experiments reported by the Mauersberger group [26, 27, 35, 36] and by Janssen and coworkers [29, 37, 38] have provided recombination rate coefficients for various types of isotopic combinations. It is the most often assumed [6, 30] that isotopic anomalies occur at the first step of the formation of the metastable complex in the Lindemann energy transfer mechanism,



followed by the stabilisation collision



with a third body M , which takes off an excess of energy to allow the complex falling down to one of the ozone po-

tential wells. The third body could be N_2 or O_2 in atmospheric conditions, or Ar in many experimental laboratory studies. Here the left-upper case indices n, m, k refer to atomic masses of the 16, 17, or 18 of oxygen isotopes (different or the same) and $N = n + m + k$ is the atomic mass of the ozone isotopologue. The asterisk means that the collision of Eq.(1) produces an excited metastable vibrational complex above the dissociation energy of the ozone potential energy surface (PES). The stabilization step of Eq.(2) depends on lifetimes of the metastable complexes (scattering resonances) that should be sufficiently long for the complex to encounter a third body before it dissociates back to atomic and diatomic fragments. There are three possible outcomes for $^N O_3^*$ after the formation step [30]: Either it dissociates to the same products at the left of Eq. (1) or to another isotopomer (isotope exchange reaction), or it can be stabilized (stabilization step). At certain pressure and temperature conditions, other reactions like the radical-complex mechanism, may also play an important role [39, 40] in ozone formation.

Janssen *et al.* [41] have found that the reaction rates for the different isotopic compositions correlates with the difference in the zero-point energies (ZPE) of various diatomic partners in Eq. (1). Marcus and co-workers [31, 42–44] have developed first theoretical models for the MIF using the RRKM theory based on certain statistical assumptions. They have shown the importance of difference Δ_{ZPE} in ZPEs of isotopologues [45] in the recombination of ozone and its isotope dependence, which was confirmed by later studies reviewed in [30] and is now considered as well understood [31]. On the contrary, the mechanism of the experimentally determined difference in the rates of formation of symmetric (such as $^{16}O^{18}O^{16}O$) versus asymmetric (such as $^{16}O^{16}O^{18}O$) ozone isotopologues was difficult to explain based on this model. To this end, Marcus and co-workers have empirically introduced the symmetry driving η -effect [31, 42, 43]. The η -effect is a non-statistical one, requiring detailed quantum calculations and making major difficulties for further theoretical interpretations.

Earlier works and related issues have been reviewed by Schinke *et al.* [30], Marcus [31]. Following the Heidenreich and Thiemens' suggestion [24] it was assumed that the observed MIF could result from lifetimes of the metastable complexes [30, 46, 47], though this idea remained controversial [48]. Since then, many theoretical studies have reported significant improvements of ab initio PESs [34, 49–52], dipole moment surface [53]. and energy level calculations [50, 54–57], as well as experimental results on laser spectroscopy measurements made for ozone isotopologues near the dissociation threshold [58–61].

The isotopic anomalies in simpler two-body oxygen isotopic exchange reactions, which can be considered as competing with the energy transfer mechanism at the stabilisation step of O_3^* have been intensively studied both experimentally [29, 62–64] and theoretically [30, 65–71].

Both experiment and the theory revealed nonstatistical behaviour of the reaction [72, 73].

Isotopic branching ratios of electronic and isotopic photodissociation channels of ozone using quantum mechanical wave packet propagation were considered in [74, 75]. The dynamics in $OO+O+Ar$ complexes was investigated to compare the temperature dependence of the ozone formation [40] with experimental data, whereas isotopic substitutions in O_3-Ar system were studied in [76]. The question whether the topological Berry phase [77] near the conical intersection in the O_3 PES should be included in the calculation of rovibronic states of the ozone molecule in its electronic ground state has been considered in [78].

Many efforts have been devoted to further theoretical modelling of the MIF processes: various possible mechanisms: Classical trajectory and quantum mechanical calculations have been carried out in groups of Schinke [30, 46, 64, 79, 80] and Babikov *et al.* [48, 81–85]. Other approaches have been reported [47, 86–90], some of them not necessarily based on the O_3^* stabilisation as discussed in [47], but a full understanding of this “strange and unconventional” [47] MIF effects is still lacking. This particularly concerns the symmetry driving effects, for which additional research is needed [82].

It is now well established [4–6] that the ozone MIF is not a minor and exotic phenomenon of a limited impact: Its effects is photochemically transferred to many oxygen-bearing species including atmospheric CO_2 , O_2 , and water in early solar system [6, 91, 92]. There is a wide area of interdisciplinary scientific fields, including atmospheric physics, geo- and cosmochemistry or climate research [5, 93–97], where the ozone isotope composition, or molecular effects of isotope fractionation, plays a major role [98–100].

The state-of-the art of the MIF studies and possible impacts in various branches of science have been described in recent exhaustive reviews by Thiemens and Lin [5], Thiemens *et al.* [20], Dauphas and Schauble [4], and Carlstad and Boering [6], who have concluded that “The origin in chemical physics of the large, robustly measured mass-independent enrichments in ozone resulting from the three-body ozone formation reaction remains elusive and represents an intriguing chemical physics puzzle that deserves further study”.

In this work we report a comparative investigation of lifetimes of the vibrational metastable $^{50}O_3^*$ ozone complex having different partial decay rates into different allowed decay channels. The $^{50}O_3^*$ complex is composed by the isotopic substitution in the main $^{48}O_3^*$ ozone with one heavy ^{18}O oxygen atom. In a simplified way, it could be viewed as being inherited from symmetric $(^{16}O^{18}O^{16}O)^*$ and asymmetric $(^{16}O^{16}O^{18}O)^*$ species, though the true picture implies some mixed variants as well. The motivation is to obtain more detailed insight into possible isotopic outcomes of the reaction (1) at the first step of ozone formation. The calculations are based on the spectroscopically accurate ab initio PES used to obtain

the metastable states above the dissociation threshold D_0 , which currently agrees the best with the observed data for the bound state levels of the ozone isotopologues [57, 60, 101, 102] up to about 95% of D_0 .

The paper is structured as follows. In the next section, the potential of ozone is discussed from a point of view of vibrational scattering states of O_3 and the method of hyperspherical coordinates with the complex absorbing potential, adapted to the theoretical description of ozone vibrational resonances. Section III is devoted to the symmetry of rovibrational resonances of ozone isotopologues. In Section IV, the results of energies, lifetimes and other observables related to the obtained vibrational resonances are presented, while in Section V different types of resonances and different decay mechanisms are discussed. Section VI concludes the article.

II. NUCLEAR DYNAMICS IN HYPERSPHERICAL COORDINATES

In its ground electronic state, ozone has an isosceles triangular equilibrium configuration, i.e. the C_{2v} point group in case of three equal oxygen isotopes. There are equivalent configurations obtained from each other by permutations of the three nuclei. Tannor [103] has demonstrated that the lowest ground state 1A_1 in the C_{2v} group can be viewed as one of the two components of the $^1E'$ electronic state of the D_{3h} group, that is degenerate at the equilateral configuration and split in the 1A_1 and 1B_2 states in the C_{2v} group by the Jahn-Teller coupling. The Jahn-Teller coupling produces three equivalent wells with three minima at the isosceles geometries. The three potential wells are separated by a large barrier, so that the lowest vibrational levels can be considered neglecting permutations of identical nuclei. However, at energies approaching the dissociation energy and above, the particle permutation should be accounted for and an accurate description of the vibrational dynamics should include the motion in the three potential wells at the same time.

Hyperspherical coordinates, in particular, the so-called democratic hyperspherical coordinates [104–109], are well suited for the description of the nuclear dynamics of the highly excited ozone molecule, as all nuclear configurations are treated on equal footing and hence the full permutational symmetry can be exploited. They are obtained by symmetrization of the three equivalent Jacobi systems. The hyperspherical coordinates provide a mapping of the nuclear configurations on a hemisphere with hyper-radius ρ , which determines the size of the three-particle system. On this hypersphere, two angles describe the shape of the triangle formed by the three particles: θ , with $0 \leq \theta \leq \pi$ is the polar angle, and ϕ , with $0 \leq \phi \leq 2\pi$ is the azimuthal angle. Pairs of configurations with θ and $\pi - \theta$ are identical, i.e. they correspond to the same distances between the three particles. Figure 1 shows how the different geometrical forms of the triangles are mapped on the upper half of the hy-

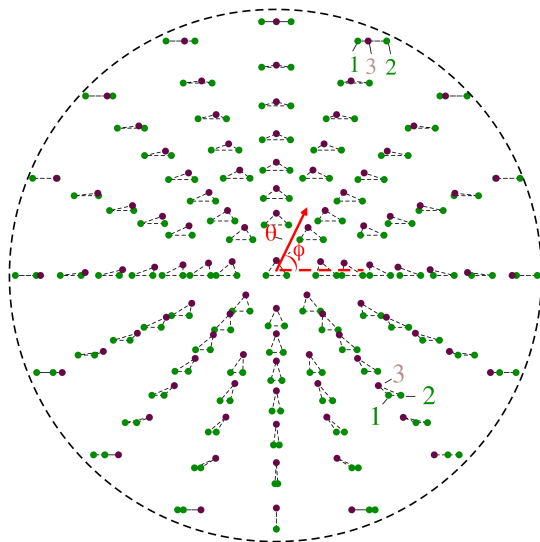


FIG. 1: Definition of the hyperangles θ and ϕ . In case of the $^{50}O_3$ ozone isotopologue the light oxygen atoms ^{16}O are shown in green color, whereas the heavy oxygen ^{18}O is in brown. The origin of the hyperspherical angle ϕ is at 03:00 h, the angle advances counter-clockwise.

persphere with $0 \leq \theta \leq \pi/2$.

The geometry of the ozone PES is illustrated in Fig. 2. On the left panel of the figure, the value of the hyper-radius $\rho = 4 a_0$ is near the minima (three equilibrium geometries) of the PES. As the hyper-radius increases beyond the value of equilibrium, the potential wells gradually disappear (middle and right panels in Fig. 2), and the three conventional configurations are no longer isolated. Three valleys show up instead that connect them (middle and right panels in Fig. 2). They represent a dioxygen molecule and a distant oxygen atom. Motion in the valley between the two colinear equatorial $\theta = \pi$ positions then describes the motion of the distant oxygen atom from one side to the other side of the diatomic molecule. This motion can be understood with the help of Fig. 1. Let us begin this analysis at the equator $\theta = \pi/2$ and $\phi = \pi/2$ or at 00:00 hours (if we use clock time notations looking at the hemisphere from above), which corresponds to the symmetric linear 132 structure, and then move clockwise. The brown atom 3, ^{18}O , then approaches atom 1, the left of the two ^{16}O in green, until at about 02:30 hours 3 and 1 are sitting upon each other. Continuing clockwise, atom 3 then overpasses atom 1, and we have the configuration 312. Passage between the linear structures at 01:00 and 04:00, while θ is changing from $\pi/2$ to somewhat smaller values and then back to $\pi/2$ (departing from the equator), approximately corresponds to a roaming motion of atom 2 around the diatomic 13, which can also be viewed as rotation of the diatomic 13 in the reference frame of the three atoms. Such a motion, departing from the equator, bypasses the singularity. Continuing clockwise, atom 1 approaches 2 until at 06:00 they are at the same position, giving rise to another singularity of the

potential. Motion around this singularity describes the roaming brown atom 3 (^{18}O). Continuing clockwise from 06:00, we find the configurations 123, and 2 approaches 3, until at about 10:00 we arrive at the third singularity, where the positions of 2 and 3 coincide. Motion around this singularity describes roaming atom 1. We finally note that all C_{2v} configurations are on the line connecting 00:00 with 06:00. The minimum of the $^{16}\text{O}^{18}\text{O}^{16}\text{O}$ isotopologue at the bottom of the PES is marked as w_3 in Fig. 2. Such a roaming motion may also be visualised in Jacobi coordinates, see Fig. 3, which are the natural coordinates to describe dissociating $\text{O}_2 + \text{O}$. A similar roaming rovibrational dynamics was previously observed in other systems, such as in H_2CO [110, 111] and CH_3NO_2 [112] and, more recently, also discussed [113] in reference to ozone.

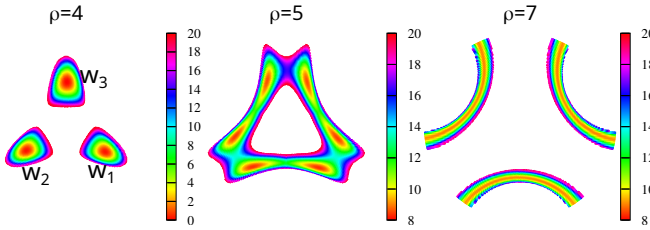


FIG. 2: The maps of the *ab initio* potential energy surface in units of 1000 cm^{-1} of the ozone molecule in the three-wells represented in a polar coordinate system for three values of the hyper-radius ρ . Possible geometrical arrangements $866 = ^{18}\text{O}^{16}\text{O}^{16}\text{O}$, $668 = ^{16}\text{O}^{16}\text{O}^{18}\text{O}$, and $686 = ^{16}\text{O}^{18}\text{O}^{16}\text{O}$ of the oxygen nuclei in the potential wells w_1 , w_2 , and w_3 correspond to conventional C_s and C_{2v} point group configurations. The left panel shows the PES cut for the near-equilibrium value of the hyper-radius $\rho = 4$ bohrs where the wells are isolated. The middle and right panels show the PES for larger values of the hyper-radius exhibiting three potential valleys for the angular (roaming) motion of the detached atom around the diatomic fragment. Another visual representation of the OO-O roaming is given by Jacobi coordinates (r_{66}, R_8, γ_8) or (r_{68}, R_6, γ_6) in Fig. 3.

To obtain wave functions, energies, and lifetimes of vibrational bound states and resonances, the approach described in Refs. [54, 105–107] was employed. Here, we give only a very brief description. The Schrödinger equation

$$[T(\rho, \theta, \phi) + V(\rho, \theta, \phi)] \Phi_v(\rho, \theta, \phi) = E_v \Phi_v(\rho, \theta, \phi). \quad (3)$$

is solved in hyperspherical coordinates in a two-step procedure. First, we solve for a number of fixed values of the hyper-radius, ρ_j ($j = 1, 2, \dots, N_\rho$), the two-dimensional angular equation

$$\left[\hbar^2 \frac{\Lambda^2 + \frac{15}{4}}{2\mu\rho_j^2} + V(\rho_j; \theta, \phi) \right] \varphi_a(\rho_j; \theta, \phi) = U_a(\rho_j) \varphi_a(\rho_j; \theta, \phi), \quad (4)$$

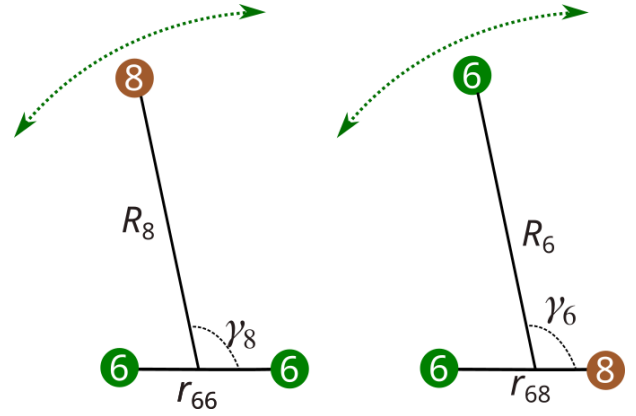


FIG. 3: Jacobi coordinates for possible roaming motion of one oxygen atom around the diatomic fragment in the vibrationally excited ozone isotopologue $^{50}\text{O}_3$ with one ^{18}O substitution. Standard abbreviated notations for the light $6 \leftrightarrow ^{16}\text{O}$ and heavy $8 \leftrightarrow ^{18}\text{O}$ oxygen atoms are used.

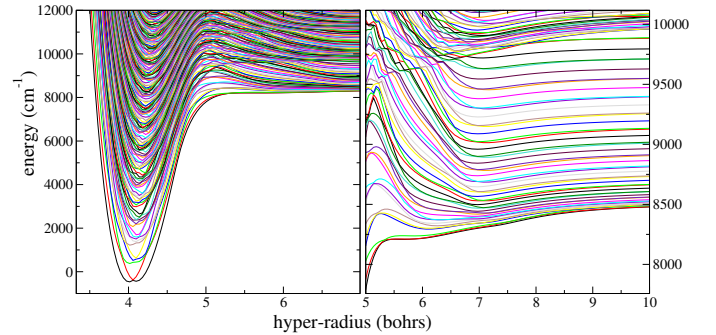


FIG. 4: Hyperspherical adiabatic curves $U_a(\rho)$ at $J = 0$ as a function of hyper-radius obtained for the $^{50}\text{O}_3$ ozone isotopologue in the first step of variational calculations, Eq. (4). In this figure, the energy origin is chosen at the ground vibrational level of $^{16}\text{O}^{18}\text{O}^{16}\text{O}$, situated 1416.602 cm^{-1} above the PES minimum. The left panel shows the global view for the adiabatic curves of the A_1 irreducible representation of the permutation-inversion symmetry group $C_{2v}(M)$. The right panel is zoomed on the region near the lowest dissociation thresholds and the asymptotic behavior at large ρ values.

where Λ^2 is the grand angular momentum squared [104, 114] and μ is the three-particle reduced mass. The solution of Eq. (4) produces adiabatic curves $U_a(\rho)$ and eigenfunctions $\varphi_a(\rho; \theta, \phi)$, defining a set of hyperspherical adiabatic (HSA) channels numerated with index a . Angular boundary conditions are employed to obtain solutions with well-defined permutational symmetry according to Section III. The lowest 240 of these curves are shown in Fig. 4. Asymptotically, different adiabatic curves correspond to various rovibrational channels of the oxygen molecules $^{16}\text{O}_2$ or $^{16}\text{O}^{18}\text{O}$ produced when O_3 dissociates. Each channel is characterized (labeled) with a label of the type of the dimer in the channel ($^{16}\text{O}_2$ or $^{16}\text{O}^{18}\text{O}$), and the rotational angular momentum j_d of the dimer, the vibrational quantum number v_d .

The wave function Φ_v in Eq. (3) is then developed as

$$\Phi_v(\rho, \theta, \phi) = \sum_a \psi_a(\rho_j) \varphi_a(\rho_j; \theta, \phi), \quad (5)$$

where $\psi_a(\rho_i)$ are ρ -dependent coefficients, which in turn are expanded in a discrete variable representation (DVR) basis $\pi_j(\rho)$, following Ref. [115],

$$\psi_a(\rho) = \sum_j c_{j,a} \pi_j(\rho). \quad (6)$$

Inserting the two above expansions into the initial Schrödinger equation (3), one obtains

$$\begin{aligned} \sum_{j',a'} \left[\langle \pi_{j'} | -\frac{\hbar^2}{2\mu} \frac{d^2}{d\rho^2} | \pi_j \rangle \mathcal{O}_{j'a',ja} + U_a(\rho_j) \delta_{j',j} \delta_{a'a} \right] c_{j'a'} \\ = E \sum_{a'} \mathcal{O}_{j'a',ja} c_{ja'} \end{aligned} \quad (7)$$

with

$$\mathcal{O}_{j'a',ja} = \langle \varphi_{a'}(\rho_{j'}; \theta, \phi) | \varphi_a(\rho_j; \theta, \phi) \rangle. \quad (8)$$

The matrix elements of the second-order derivative with respect to ρ in the above equation are calculated analytically (see, for example, [116, 117] and references therein). To obtain the continuum solutions, a complex absorbing potential was added at large ρ -values [106].

The convergence tests for obtained energies and lifetimes were performed. The parameters, to which the energies and lifetimes are sensitive the most, are the numbers (N_θ , N_ϕ , N_ρ) of basis functions in hyperspherical coordinates, the number N_a of adiabatic states in the expansion of Eq. (5), and the position ρ_c , the strength V_c , and the length L_c of the complex absorbing potential. Having performed the convergence tests, we found the values $N_\theta=120$, $N_\phi=300$, $N_\rho=200$, $N_a=180$, $\rho_c=9$ bohrs, $V_c=0.005$ hartree, $L_c=6$ bohrs provide convergence for energies of the resonances with uncertainty of about 0.2 cm^{-1} , and for the relative uncertainty of lifetimes of about 0.2%. The uncertainty in energies of calculated bound states is much better than 0.2 cm^{-1} , it is of the order of 10^{-4} cm^{-1} .

Looking at wave functions of vibrational states gives an intuition about motion in hyperspherical coordinates. An example of such wave functions is shown in Fig. 5, where the hyper-angular dependence at a fixed value of $\rho = 9$ bohrs of a state with energy $E = 8542.82 \text{ cm}^{-1}$ is demonstrated. Green circles refer to the ^{16}O isotopes and brown circles to the heavy ^{18}O isotope. At the right PES valley, the Jacobi angle γ_6 of the rotation of ^{16}O around the $^{18}\text{O}^{16}\text{O}$ diatomic fragment varies from 0 to π , whereas the average value of the hyperangle is $\langle \phi \rangle = 30^\circ$.

Symbols w_1 , w_2 and w_3 in Fig. 5 mark minima of the three potential wells (situated at a smaller hyper-radius, $\rho \sim 4.2$ bohrs). At this relatively large value of the hyper-radius $\rho = 9$ bohrs (see also Fig. 4), one of the three atoms is almost uncoupled from the diatomic

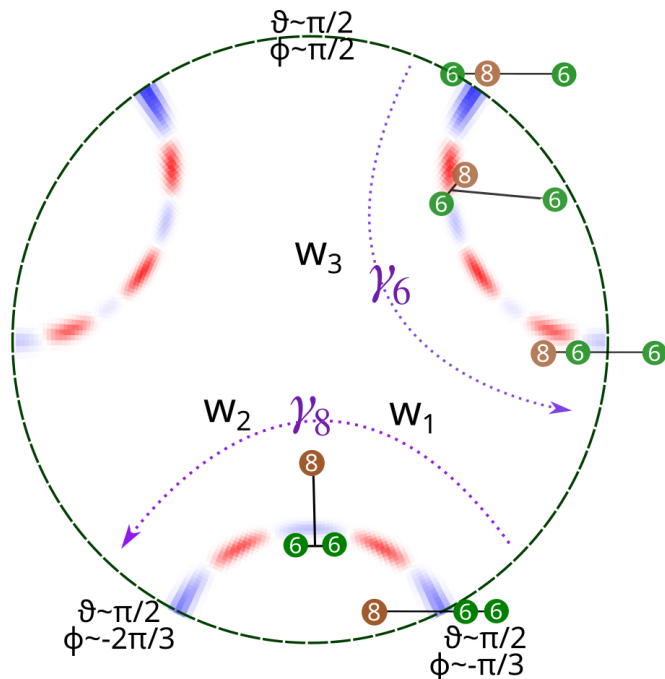


FIG. 5: The figure shows the hyper-angular dependence of the wave function of the state with energy $E = 8542.82$ at $\rho = 9$ bohrs. Symbols w_1 , w_2 and w_3 mark equilibrium locations of the potential wells. Classical roaming $^{16}\text{O}^{16}\text{O} - ^{18}\text{O}$ corresponds to nodal lines (red and blue areas) of the wave function. Green circles mark positions of the light ^{16}O isotopes and brown circles of the heavy ^{18}O isotope. The Jacobi angle γ_8 of the rotation of ^{18}O around the $^{16}\text{O}^{16}\text{O}$ diatomic fragment varies from 0 to π .

molecule. Classical roaming motion of an atom around the O_2 dimer is clearly represented by nodal structures (red and blue areas in the figure) in three sectors of the complete hyperangular space (the PES valleys). The fact that the wave function is not negligible in all three sections means that the motion is delocalised in the three channels, corresponding to the three asymptotic arrangements: $^{16}\text{O}-^{16}\text{O}^{18}\text{O}$ and $^{18}\text{O}-^{16}\text{O}_2$, with the first one being doubly-degenerate. The wave function in the left PES valley, near 9:00-11:00, is the same as in the right one, 1:00-3:00, because the two valleys are obtained from each other by a permutation of the identical ^{16}O atoms. The valley at the bottom, near 5:00-7:00, corresponds to the ^{18}O atom separated from $^{16}\text{O}_2$. The wave function in this region is not the same as in the two other valleys. Nodes of the wave function in the three valleys are aligned mainly along the ϕ coordinate and not perpendicular to it. This indicates that the diatomic O_2 is in its vibrational ground state.

In contrast to the wave function of Fig. 5 with the ground vibrational level of O_2 in all three dissociation channels, Fig. 6 gives an example of the state with the wave function having in the two $^{16}\text{O} + ^{16}\text{O}^{18}\text{O}$ valleys (9:00-11:00 and 1:00-3:00) a node perpendicular to ϕ and mainly along the θ coordinate. A node along θ corre-

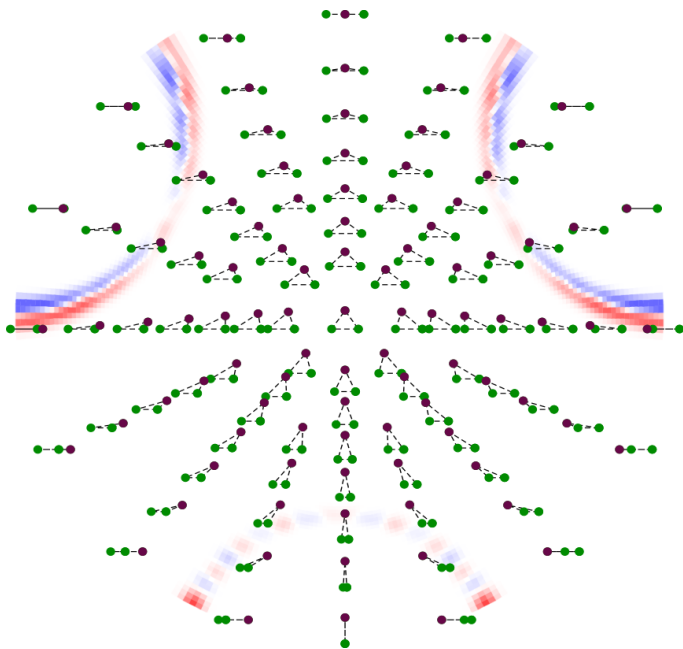


FIG. 6: Wave function (red and blue areas) of a resonant state with energy 9955 cm^{-1} shown in the hyperangular coordinates in the dissociation region at a large $\rho=9$ bohrs. This state decays partially to the $^{16}\text{O} + ^{16}\text{O}^{18}\text{O}$ ($v = 1, j = 0$) channel and partially to $^{18}\text{O} + ^{16}\text{O}_2$ ($v = 0, j = 16$). The nodal structure along the ϕ coordinate in the lower valley ($^{18}\text{O} + ^{16}\text{O}_2$) is due to the highly excited $j = 16$ rotational state of the $^{16}\text{O}_2$ dimer, while a node along the θ coordinate in the two upper valleys ($^{16}\text{O} + ^{16}\text{O}^{18}\text{O}$) is due to the vibrationally excited state of the dissociating dimer. The background picture with small triangles is the same as in Fig. 1 and helps to associate geometries of the three atoms with the amplitude of the wave function.

sponds to the vibrating ($v = 1$) O_2 molecules. As one can also see, in the lower valley (5:00-7:00), that the motion is just roaming, i.e. the relative rotation of ^{18}O and $^{16}\text{O}_2$. This state is a resonance state with energy 9955 cm^{-1} , which decays partially to the $^{16}\text{O} + ^{16}\text{O}^{18}\text{O}$ ($v = 1, j = 0$) channel and partially to $^{18}\text{O} + ^{16}\text{O}_2$ ($v = 0, j = 16$). Amplitudes in other symmetry-allowed channels are significantly smaller.

The wave function of that state is also shown in Fig. 7 in a different form: by surfaces of a constant amplitude (positive - red color, negative - blue color) in all three hyperspherical dimensions ρ, θ, ϕ . The three hyperspherical coordinates are arranged in the same way as in a familiar arrangement of standard spherical coordinates, i.e. ρ corresponds to the distance from the center of the coordinate system, the angles θ and ϕ represent polar and azimuthal angles of orientation in a Cartesian coordinate system with axes x, y , and z . Therefore, the dissociation region in this picture corresponds to large distances from the origin, the minima of the potential $w_{1,2,3}$ are around $\rho = 4$ a.u. The upper part of the figure is the view from “above” the hypersphere, along the z axis down to the xy plane, while the lower part of the figure is a view at a cer-

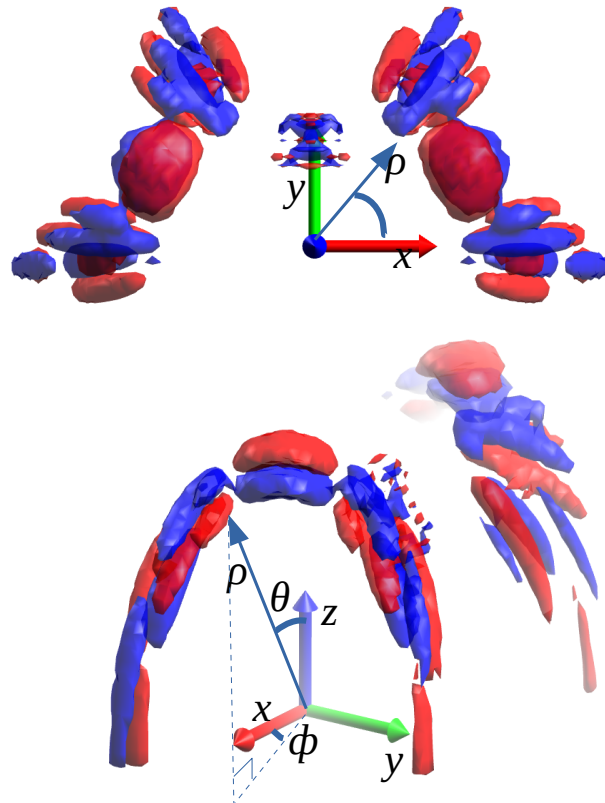


FIG. 7: Wave function (red and blue areas) of a resonant state with energy 9955 cm^{-1} (same as in Fig. 6) shown in the three hyperspherical coordinates. The lifetime of this resonance is $\tau = 210$ ps.

tain arbitrary orientation with respect to the coordinate frame. The back side of the wave function is partially hidden (the “fog” effect) to help understanding relative positions of different nodal structures of the wave function. This way of representing wave functions is also used in other figures below.

III. SYMMETRY PROPERTIES OF THE ROVIBRONIC WAVE FUNCTIONS

The rovibrational states of $^{16}\text{O}^{18}\text{O}^{16}\text{O}$ and $^{16}\text{O}^{16}\text{O}^{18}\text{O}$ are traditionally classified according to the point groups C_{2v} and C_s , respectively. The vibrational modes and their symmetry labels are for $^{16}\text{O}^{18}\text{O}^{16}\text{O}$ the symmetric stretch, ν_1 (A_1), the bending, ν_2 (A_1), and the antisymmetric stretch, ν_3 (B_1), modes. For $^{16}\text{O}^{16}\text{O}^{18}\text{O}$, ν_1 denotes the $^{16}\text{O} - ^{16}\text{O}$ stretch, ν_2 the bending and ν_3 the $^{16}\text{O} - ^{18}\text{O}$ stretch modes, they all have symmetry A' .

Separating the $^{16}\text{O}^{18}\text{O}^{16}\text{O}$ and $^{16}\text{O}^{16}\text{O}^{18}\text{O}$ species is appropriate only if the energy of the molecule is near the bottom of the potential well. In our previous work [57],

TABLE I: Character table of the point group C_{2v} , the diatomic molecule point groups $D_{\infty h}$ and $C_{\infty v}$ (excerpts) and the permutation inversion group $S_2 \times I$ using the nomenclatures of $C_{2v}(M)$, $D_{\infty h}(M)$ and $C_{\infty v}(M)$ for the irreducible representations.

C_{2v}			E	C_{2b}	σ_{ab}	σ_{bc}	
$D_{\infty h}$			E	$\infty C'_2$	$\infty \sigma_v$	i	
$C_{\infty v}$			E		$\infty \sigma_v$		
$S_2 \times I$			E	(12)	E^*	(12)*	
$C_{2v}(M)$	$D_{\infty h}(M)$	$C_{\infty v}(M)$					
A_1	Σ_g^+	Σ^+	1	1	1	1	$p_b (p_x)$
B_1	Σ_u^+		1	-1	1	-1	$p_a (p_z)$
A_2	Σ_u^-	Σ^-	1	1	-1	-1	
B_2	Σ_g^-		1	-1	-1	1	$p_c (p_y)$

we have shown that the motion of the molecule is delocalised even below the dissociation threshold, so that $^{16}\text{O}^{18}\text{O}^{16}\text{O}$ and $^{16}\text{O}^{16}\text{O}^{18}\text{O}$ cannot be separated in classification of rovibrational states. A more rigorous symmetry classification is obtained within the two-particle permutation inversion group, $S_2 \times I$. This group is isomorphic with the point group C_{2v} and may also be referred to as molecular symmetry group $C_{2v}(M)$. The irreducible representations of this group are presented in Table I. We note here that the molecule is placed in the xz plane, which is the convention normally used in ozone spectroscopy [122]. The correspondence between the principal axes of inertia, a, b, c , and the Cartesian axes, x, y, z , is thus ($x \rightarrow b, y \rightarrow c, z \rightarrow a$), which is the I_r representation.

The pure vibrational modes are invariant with respect to an inversion of the spatial coordinate system, the operator E^* , hence they must be either A_1 or B_1 . The symmetry of the three modes of $^{16}\text{O}^{16}\text{O}^{18}\text{O}$ are thus A_1 in $C_{2v}(M)$. Two equivalent forms exist of $^{16}\text{O}^{16}\text{O}^{18}\text{O}$, $^{16}\text{O}_{[1]}^{16}\text{O}_{[2]}^{18}\text{O}$ and $^{16}\text{O}_{[2]}^{16}\text{O}_{[1]}^{18}\text{O}$, located in the wells w_1 and w_2 . Their vibrational functions will be denoted $|v_1 v_2 v_3\rangle_1$ and $|v_1 v_2 v_3\rangle_2$, respectively. The corresponding configurations are indistinguishable and should, therefore, be symmetrized within $C_{2v}(M)$. Non-symmetrized wave functions are approximate and can be used only if the energy is much lower than the potential barrier between the w_1 and w_2 wells. The symmetrization yields the two linear combinations

$$|v_1 v_2 v_3; \pm\rangle_{668} = N_{\pm} (|v_1 v_2 v_3\rangle_1 \pm |v_1 v_2 v_3\rangle_2). \quad (9)$$

N_{\pm} are normalization constants. Deep in the potential wells, where tunneling can be neglected, they are $N_{\pm} = 1/\sqrt{2}$. The two functions are symmetric ($|v_1 v_2 v_3; +\rangle_{668}$) and anti-symmetric ($|v_1 v_2 v_3; -\rangle_{668}$) with respect to permutation of the two ^{16}O nuclei, operator (12), and transform as A_1 and B_1 .

The vibrational functions of the $^{16}\text{O}^{18}\text{O}^{16}\text{O}$ isomer $|v_1 v_2 v_3\rangle_{686}$ are already symmetry-adapted and transform as A_1 for even values of the anti-symmetric stretch quantum number v_3 and B_1 for odd values of v_3 .

The rovibrational basis functions $|v_1 v_2 v_3 JK_a K_c\rangle$ are

TABLE II: Symmetry classification of rovibrational states in $S_2 \times I$ and their statistical weights.

configuration	v_3	K_a, K_c			
		ee	eo	oe	oo
668+	-	$A_1 (1)$	$B_2 (0)$	$B_1 (0)$	$A_2 (1)$
668-	-	$B_1 (0)$	$A_2 (1)$	$A_1 (1)$	$B_2 (0)$
686	even	$A_1 (1)$	$B_2 (0)$	$B_1 (0)$	$A_2 (1)$
686	odd	$B_1 (0)$	$A_2 (1)$	$A_1 (1)$	$B_2 (0)$

written as

$$|v_1 v_2 v_3 JK_a K_c; \pm\rangle_{668} = |v_1 v_2 v_3; \pm\rangle_{668} |JK_a K_c\rangle, \quad (10)$$

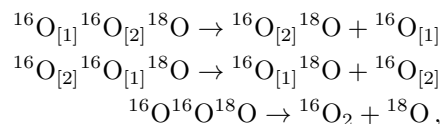
$$|v_1 v_2 v_3 JK_a K_c\rangle_{686} = |v_1 v_2 v_3\rangle_{686} |JK_a K_c\rangle, \quad (11)$$

where $|JK_a K_c\rangle$ are asymmetric top rotational functions, and K_a and K_c are the quantum numbers for the internal projections of the total angular momentum on the a and c axes, $K_{a,c} = |k_{a,c}|$. The symmetry species of the rotational functions depend on whether the K -values are even (e) or odd (o), respectively, and are A_1 for $(K_a, K_c) = ee$, B_2 for $(K_a, K_c) = eo$, B_1 for $(K_a, K_c) = oe$, and A_2 for $(K_a, K_c) = oo$ in the present axis convention.

Not all of the rovibrational functions are physically allowed. ^{16}O (and also ^{18}O) are bosons with nuclear spin $i = 0$, and hence only rovibrational functions of symmetry A_1 or A_2 are possible, given that the electronic wave function of the X^1A_1 state is totally symmetric. The symmetry classification of the rovibrational states and their spin-statistical weights are given in Table II. We note here that tunnelling splitting cannot be observed directly, as one of the functions of the \pm -pair in Eq. (10) is always symmetry forbidden due to vanishing spin weight. However, the energy difference of the two band origins may be estimated from the allowed $J = 1$ levels under the assumption that the values of the rotational constants are the same.

At high energies, where the three potential wells are not isolated, a distinction between $^{16}\text{O}^{18}\text{O}^{16}\text{O}$ and $^{16}\text{O}^{16}\text{O}^{18}\text{O}$ is no longer possible and their approximate spectroscopic quantum numbers do not hold anymore. The resulting states can be labelled rigorously by their symmetry, Γ , rotational quantum number, J , and a counting index n . An example of such a state delocalised between different configurations is shown in Fig. 6.

In our publication [54] on $^{16}\text{O}_3$ we have shown that purely vibrational, i.e. $J = 0$ resonance states of $^{16}\text{O}_3$ cannot decay into $\text{O}_2 + \text{O}$ with an outgoing $l = 0$ partial wave on the electronic ground state surface as such a process is symmetry-forbidden. We shall now analyse the situation for the ^{18}O -enriched ozone, for which the three decay channels, $\kappa = 1, 2, 3$, are possible:



where the first and second channels lead to identical products.

The asymptotic wave function in the exit channel κ , where κ corresponds to the index of the separating atom, can be expressed in Jacobi coordinates as [118]

$$\Psi_{\kappa v_d j l}^{JM}(\vec{r}_\kappa, \vec{R}_\kappa) \approx \frac{1}{r_\kappa R_\kappa} \varphi_a^{el} \varphi_d^{el} \chi_{v_d j}(r_\kappa) \mathcal{Y}_{j l}^{JM}(\hat{r}_\kappa, \hat{R}_\kappa) e^{i(kR_\kappa - l\pi/2)}, \quad (12)$$

where $\exp(i(kR_\kappa - l\pi/2))$ is the scattering function of the outgoing wave and $\chi_{v_d j}(r_\kappa)$ the rovibrational wave function of the O_2 molecule; r_κ and R_κ are the true, not mass-scaled, distances in the Jacobi coordinate system κ . M is the external projection of J . Functions φ_a^{el} and φ_d^{el} represent electronic states of the oxygen atom and the dioxygen molecule. $\mathcal{Y}_{j l}^{JM}$ are the bipolar harmonics [119], that couple the angular momentum, j , of the dioxygen molecule with the angular momentum, l , of the atom-diatom relative motion, to yield the total angular momentum, J . They are defined as

$$\mathcal{Y}_{j l}^{JM}(\hat{r}_\kappa, \hat{R}_\kappa) = \sum_{m_l, m_j} C_{j m_j l m_l}^{JM} Y_{j m_j}(\hat{r}_\kappa) Y_{l m_l}(\hat{R}_\kappa), \quad (13)$$

where the Y are spherical harmonics and C are Clebsch-Gordan coefficients.

Let us consider first the channel $^{16}O^{16}O^{18}O \rightarrow ^{16}O_2 + ^{18}O$, i.e. $\kappa = 3$, corresponding to the valley at the lower part of Fig. 5 with the increasing ρ . The electronic ground state of dioxygen is $X^3\Sigma_g^-$, that of the oxygen atom is 3P . In our paper [54], we have examined the case $^{16}O_3$. According to Table I, the electronic wave function of dioxygen transforms as B_2 in $C_{2v}(M)$. The three p -orbitals of the oxygen atom, of which two are singly occupied to form a triplet state, transform as A_1 , B_2 and B_1 , respectively, in this group, and there is a microconfiguration, $p_a^2 p_b p_c$ that has $B_1^2 \times A_1 \times B_2 = B_2$ symmetry just as the electronic wave function of the dioxygen molecule. Their product has A_1 symmetry, and hence they can dissociate on the ground state surface of ozone as far as electronic symmetry is concerned.

In fact, the product of the two electronic functions $\varphi_a^{el} \varphi_d^{el}$ in Eq. (12) must always be symmetric, because within the Born-Oppenheimer approximation the potential energy surface of the triatomic ozone, \tilde{X}^3A' , is symmetric with respect to an exchange of any two nuclei, irrespective of their isotopic masses. In the case of $^{16}O^{16}O^{18}O$, this may also be rationalized as follows: Permutation of the two ^{16}O nuclei rotates the molecular plane by π , and hence the perpendicular p_c atomic orbital changes its phase, as does the bipolar harmonic. The product of the electronic functions remains symmetric. The vibrational wave function of $^{16}O_2$ is symmetric, and only rotational states with odd values of j exist, such that the product $\varphi_d^{el} \chi_{v_d j}(r_{\kappa=3})$ is symmetric with respect to (12). Dissociation $^{16}O^{16}O^{18}O \rightarrow ^{16}O_2 + ^{18}O$ with $J = 0$ implies an $l = 1$ partial wave of the outgoing oxygen atom.

The asymptotic functions of Eq. (12) for the channels $\kappa = 1, 2$ do not belong to a definite representation of

$C_{2v}(M)$. The permutation operator (12) when applied to one of those functions interchanges the ^{16}O nuclei of the $^{16}O^{18}O$ molecule and the free atom, so that

$$(12)\Psi_{\kappa=(1,2)v_d j l}^{JM}(\vec{r}_\kappa, \vec{R}_\kappa) = \Psi_{\kappa=(2,1)v_d j l}^{JM}(\vec{r}_\kappa, \vec{R}_\kappa). \quad (14)$$

The symmetric linear combination of the functions with $\kappa = 1$ and $\kappa = 2$ then transforms as A_1 in $C_{2v}(M)$. This result is expected as the products of the two channels are indistinguishable. There are no restrictions on the total angular momentum J , since for $^{16}O^{18}O$ both even and odd values of j are possible.

IV. ENERGIES AND LIFETIMES OF VIBRATIONAL RESONANCES

We have computed $J = 0$ states above the dissociation threshold both in symmetry A_1 and B_1 up to 13000 cm^{-1} . B_1 -states are not allowed, but their $J = 0$ energy values represent the origins of the 668- and 686 (v_3 odd) rovibrational bands, for which states with $J > 0$ do exist (see Table II). It is then instructive to compute the corresponding band origins because they are well determined in experimental spectra analyses [102] using interpolations of series of rotational lines to the $J \rightarrow 0$ limit. The character of these states can be understood from Fig. 8, which shows the expectation value of the hyperangle ϕ , $\langle \phi \rangle = \langle \Psi | \phi | \Psi \rangle$ as function of the energy. For both A_1 and B_1 states, the probability density is the same in the equivalent wells w_1 and w_2 , so the integral $\langle \phi \rangle = \langle \Psi | \phi | \Psi \rangle$ is evaluated only over the half of the whole interval of ϕ , in the range $-90^\circ \leq \phi \leq 90^\circ$ and then multiplied by two. Evaluating the integral over the whole interval $[-\pi/2; 3\pi/2]$ of variation of ϕ would give an expectation value corresponding the averaged value for positions for the two equivalent wells and, therefore, would not allow to "see" where the states are primary localized. As one can see from the figure, the states with energies below the dissociation threshold of $O_2 + O$, $D_0 = 8500 \text{ cm}^{-1}$ are localised in one of the wells, either $w_1(\phi = -30^\circ)$, equivalent to w_2 , or in $w_3(\phi = 90^\circ)$. In traditional analyses of experimental spectra [102] (and references therein), these states with the expectation value around $\phi \approx 90^\circ$ are classified using the C_{2v} point group, while the states with $\phi \approx -30^\circ$ are classified using the C_s point group. At energies approaching D_0 , the expectation value is departing from one of the two values $\phi = 90^\circ$ or -30° , indicating the highly-excited bound states and the states above (vibrational continuum states) are delocalised between the three wells. We notice, however, that some states at energies above D_0 remain localised at geometries near one of the wells. These metastable states continue the series of bound vibrational resonances of highly excited bending or symmetric stretch vibrational modes, which become metastable above the dissociation limit.

The computed lifetimes of the continuum states vary by several orders of magnitude, between 0.01 ps and

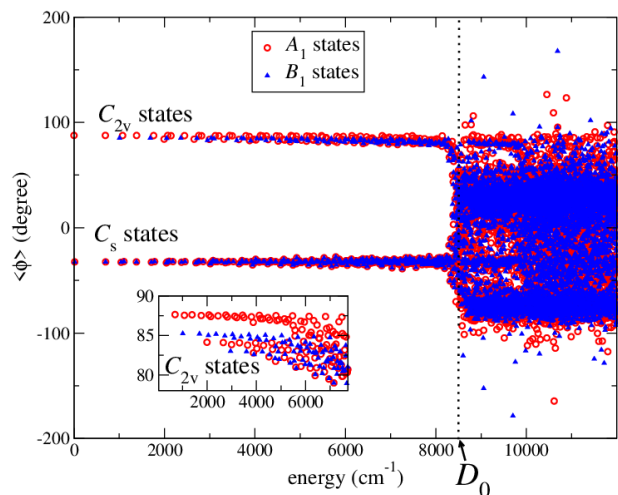


FIG. 8: Average values $\langle \Psi | \phi | \Psi \rangle$ of the hyperangle ϕ computed for the $^{50}\text{O}_3$ ozone isotopologues, both for the bound and metastable states. The dissociation energy threshold $D_0 \approx 8500 \text{ cm}^{-1}$ is marked by a dotted vertical line. The states with energies below D_0 are localised in one of the wells, either in w_1 ($\phi = -30^\circ$) equivalent to w_2 , or in w_3 ($\phi = 90^\circ$). At energies near and above D_0 , the expectation value for the majority of the states is different than $\phi = 90^\circ$ or -30° . These states are not localised in one of the wells.

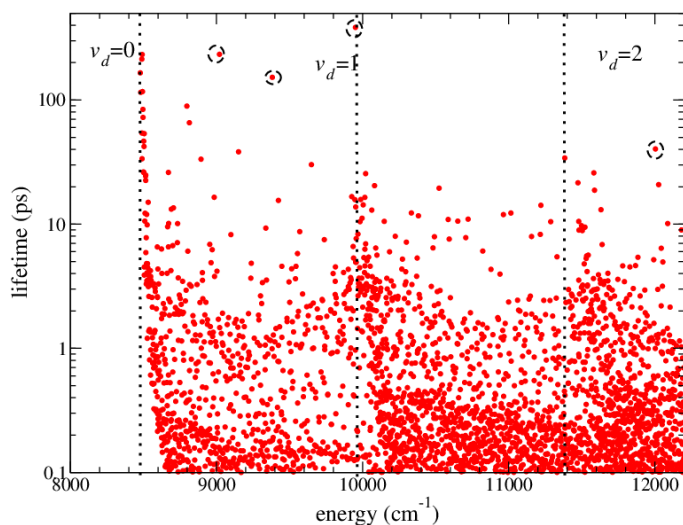


FIG. 9: Overall picture of lifetimes of A_1 states as a function of state energy. The vertical dotted lines refer approximately to the threshold energies for excitation of the O_2 dimer in the dissociation channels, $v_d = 0, 1$, and 2 .

300 ps. The lifetimes of the A_1 states are shown in Figs. 9, 10, and 11. The overall picture of lifetimes of A_1 states is shown in Fig. 9. The vertical dotted lines indicate the threshold energies for excitation of the O_2 dimer in the dissociation channels, $v_d = 0, 1$, and 2 . For each v_d there are two thresholds close to each other and corresponding to the two different isotopologues $^{16}\text{O}^{16}\text{O}$ and $^{16}\text{O}^{18}\text{O}$.

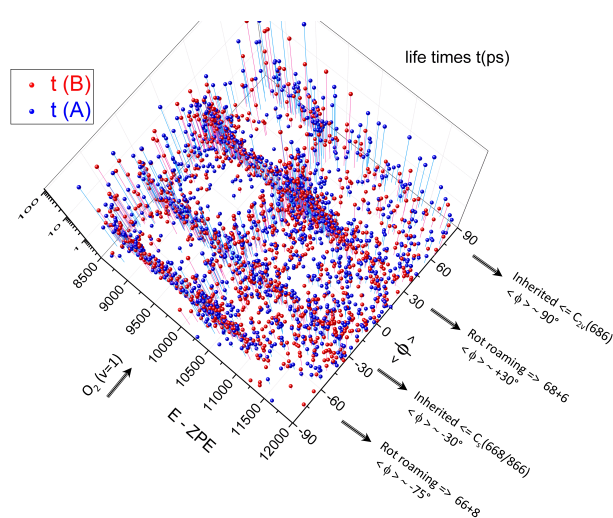


FIG. 10: Lifetimes of the vibrational resonances of the $^{50}\text{O}_3$ isotopologues as a function of the energies E the expectation value of the hyperangle $\langle \phi \rangle$. Several series clearly appear, which correspond to physically different types of the metastable states.

The states with lifetimes around and smaller than 0.1 ps should not be considered as resonances. They are rather simple vibrational continuum states, corresponding to $\text{O}+\text{O}_2$ half-collisions. On the other hand, vibrational resonances having very different lifetimes, as demonstrated in Fig. 9 should have different character and different decay mechanisms.

To understand how lifetimes τ of the states are related to the type of the resonances, it is useful to consider the dependence of the lifetimes vs energy and the averaged values $\langle \phi \rangle$, $\langle \rho \rangle$. Strictly speaking, for vibrational resonances (as well as for simple vibrational continuum states), the expectation value of the hyper-radius is undefined. However, if one limits the interval of integration over ρ by some large, but a finite value (such as in the present numerical calculations), the expectation value $\langle \rho \rangle$ can characterize the overall size in ρ of different resonances – not absolutely – but relative to each other. At the same time, evaluating the integral $\langle \phi \rangle$ in same way, allows us to analyse the short-distance character of the states with respect to localisation in or outside of the three potential wells. Figure 10 shows the dependence $\tau(E, \langle \phi \rangle)$ as a function of energy and $\langle \phi \rangle$ and Fig. 11 demonstrates the dependence $\tau(E, \langle \rho \rangle)$ for the metastable states for relatively small size of the complex.

One can see from Fig. 11 that states with $\langle \rho \rangle \lesssim 4.8$ bohrs tend to have bigger lifetimes than states with larger $\langle \rho \rangle$. At such values of $\langle \rho \rangle \lesssim 4.8$ bohrs, the potential wells are still present, but are already communicating, as can be seen from Figure 2. Such resonances are metastable vibrational states of the ozone molecule. As the size of the triatomic system increases, we find states with very short lifetimes. These states are generally localised in the

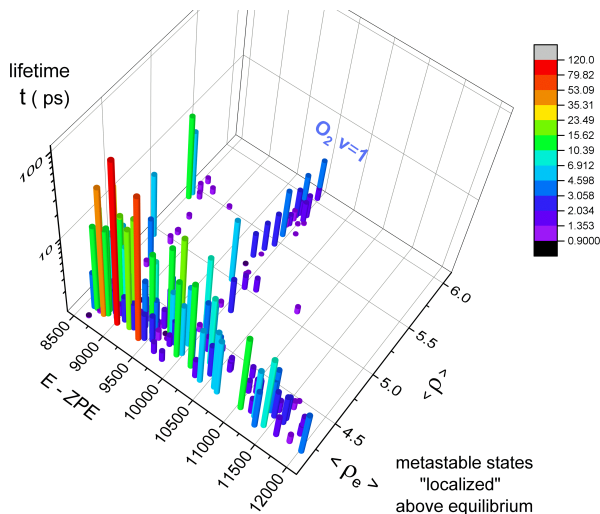


FIG. 11: Lifetimes as a function of the energies E and of the expectation value of the hyper-radius $\langle\rho\rangle$. States with $\langle\rho\rangle < 6$ a.u. are shown only.

$\text{O}_2 + \text{O}$ channels, which are formed at large ρ . Their character resembles more to a simple vibrational continuum state and less to a scattering resonance.

Inspecting Fig. 10, showing $\tau(E, \langle\phi\rangle)$, we notice that the largest lifetimes are found for states with low energy and $\langle\phi\rangle \approx 90^\circ$, which are C_{2v} series at the potential well w_3 of the $^{16}\text{O}^{18}\text{O}^{16}\text{O}$ isotopologue. They inherited from the metastable $^{16}\text{O}^{18}\text{O}^{16}\text{O}$ states that have to transfer vibrational energy to the antisymmetric mode in order to decay. The states with $\langle\phi\rangle \approx -30^\circ$ are resonances of a similar type, but sitting above the potential wells w_1 and w_2 . They have smaller lifetimes than the former states, which reflects the fact that they are delocalised over two equivalent wells. The states with $\phi \approx -75^\circ$ and $\phi \approx 30^\circ$ are the roaming states, decaying into $^{16}\text{O}_2 + ^{18}\text{O}$ and $^{16}\text{O}^{18}\text{O} + ^{16}\text{O}$, respectively. States with relatively large lifetimes appear at the threshold energy of O_2 with $v_d = 1$ vibrational excitation. The states above this threshold are in the O_2 , $v_d = 0$ continuum and are thus vibrational Feshbach resonances. They decay transferring the vibrational energy of the dimer into the kinetic energy of the $\text{O}_2 + \text{O}$ products. Typical resonances of each type are discussed below.

V. DIFFERENT TYPES OF RESONANCES: DIFFERENT DECAY MECHANISMS

Averaged values of ρ and ϕ give an idea about localization of a particular vibrational resonance. Looking at the wave function of that state helps to understand to which classical motion of the three oxygen atoms the state corresponds. In this respect, there are several distinct types of resonances.

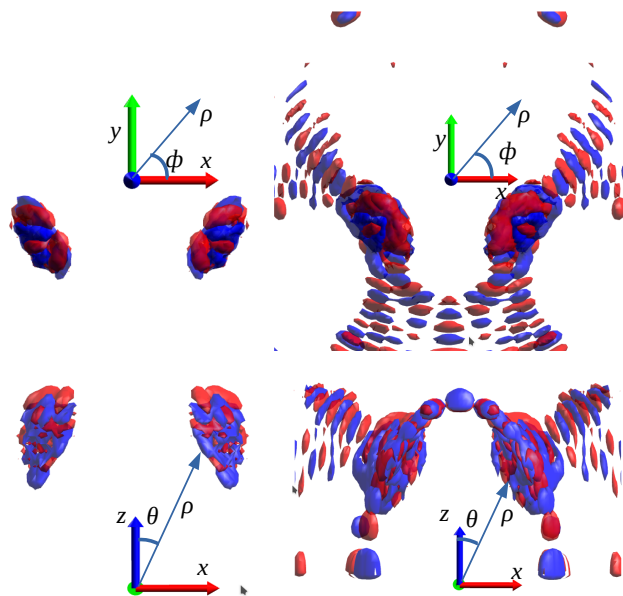


FIG. 12: The vibrational resonance with $E = 8815.3 \text{ cm}^{-1}$, $\tau = 33 \text{ ps}$, localized at small distances between O_2 and O , primarily at the 668/866 geometrical arrangements, i.e. above the w_1 and w_2 wells. The wave function is drawn for the isosurface values of 0.02 (the two plots on the left) and 0.001 (the two plots on the right).

A. Resonances localized in the C_s potential wells

Vibrational motion of bound states at low energies is well described by the normal mode approximation in each of the $w_{1,2}$ and w_3 wells, so that the wave function of each low-energy bound state is characterized by three quantum numbers of vibrational modes and a label whether the molecule is symmetric w_3 or not $w_{1,2}$. Vibrational levels in the same well differing by only one of the three quantum numbers form series of states with similar character of motion. At energies, approaching the dissociation limit, the normal mode approximation is, strictly speaking, not applicable. However, if the molecule stays the most of the time (in a classical description) at geometries near the minimum of the potential, the normal-mode character of such states near the dissociation region is conserved. Such quantum states are present below and above the dissociative limit. They could be viewed as continuations of the corresponding low-energy normal-mode series mentioned above.

An example of such a resonance, which is mostly localized in asymmetric wells $w_{1,2}$, is shown in Fig. 12. The figure shows the wave function of the resonance by two isosurfaces, one at the value of 0.02 (two orthogonal projections xy and xz on the left) and at the value of 0.001 (similar orthogonal plots on the right). One can see at

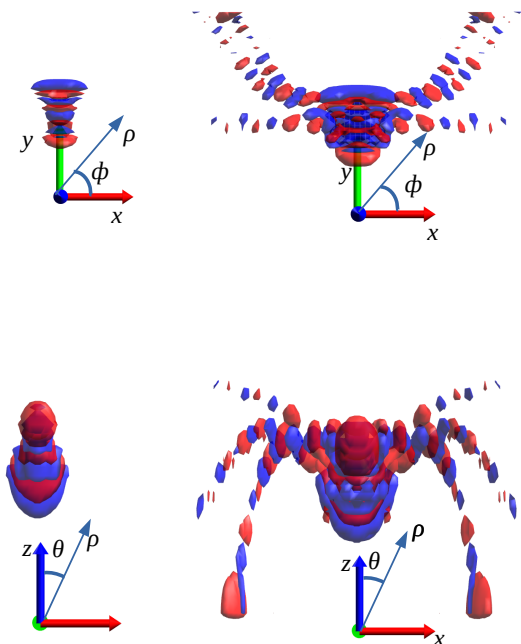


FIG. 13: The vibrational resonance with $E = 8797.59 \text{ cm}^{-1}$, $\tau = 45 \text{ ps}$, localized at small distances between O_2 and O primarily at the 686 geometrical arrangement, i.e. above the w_3 well. The wave function is shown for the isosurface values of 0.02 (the two plots on the left) and 0.002 (the two plots on the right). The small-distance vibrational motion (the left plots) is a pure bending mode with 13 quanta in the mode $v_b = 13$.

the higher value of the isosurface, the resonance is localised in the w_1 and w_2 asymmetric wells, very similar to how bound states look like. From the upper right plot – the orthogonal xy projection at the smaller amplitude value – it is evident that the wave function is oscillating at large distances ρ and present in all decay channels $^{16}\text{O}_2 + ^{18}\text{O}$ and $^{16}\text{O}^{18}\text{O} + ^{16}\text{O}$, therefore, indicating that the resonance decays to the symmetric and asymmetric channels with comparable probabilities.

B. Resonances localized in the C_{2v} potential well

The second type of resonances is the continuation of series of normal-mode bound states localized in the symmetric well w_3 . Wave function of two such resonances are shown in Figs. 13 and 14. Figure 13 shows the resonance of a pure bending mode with 13 quanta in the mode $v_b = 13$ in the symmetric well and energy 300 cm^{-1} above the dissociative limit. The states with a smaller number of quanta $v_b = 0-12$ are bound. Such pure-bending states have the nodal structure aligned mainly along the θ coordinate near $\phi = \pi/2$. The motion along θ corresponds to the bending motion. A noticeable feature of the wave function is the dominance of the asymmetric

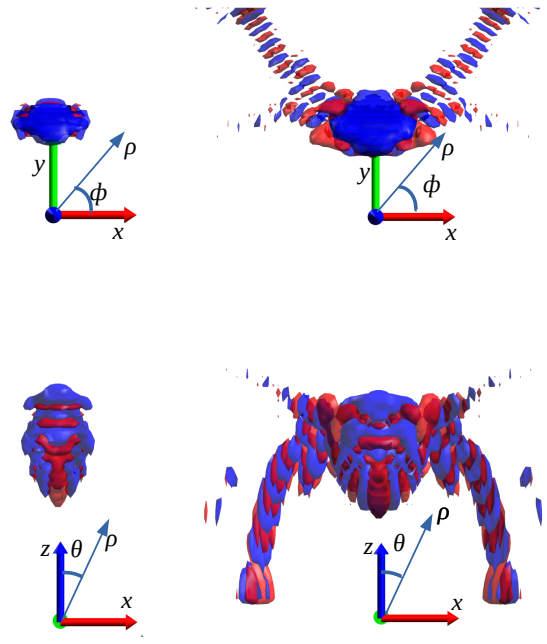


FIG. 14: Another example of a resonance – similar to the one in Fig. 13 – localized at small distances at the 686 arrangement with $E = 9385.37 \text{ cm}^{-1}$, $\tau = 72 \text{ ps}$. The isosurface values are 0.01 (the two plots on the left) and 0.001 (the two plots on the right). It is a pure symmetric-stretching-mode resonance with 9 quanta in the mode $v_{ss} = 9$.

decay channel: On the upper right plot – the xy view – the smaller-amplitude nodal structure is negligible in the $^{18}\text{O} + ^{16}\text{O}_2$ channel. This is not surprising because it is more difficult to separate ^{18}O than ^{16}O in the symmetric molecule $^{16}\text{O}^{18}\text{O}^{16}\text{O}$.

Figure 14 gives the wave function of the pure symmetric-stretching-mode resonance with 9 quanta in the mode $v_{ss} = 9$. The symmetric stretching motion corresponds approximately to the change in the hyper-radius only. Similarly to the wave function in Fig. 13, the asymmetric decay channels are dominant.

The resonances localized above the potential wells have lifetimes of the order $\gtrsim 10 \text{ ps}$.

C. Rotational roaming

Figure 5 is an example of another type of resonances, the rotational roaming states. Such states could be viewed as weakly-bound $\text{O}_2 + \text{O}$ complexes where the two fragments O_2 and O rotate around each other or, looking from the molecular frame, the O_2 molecule rotates with respect to the vector pointing to the O atom. The fragments stay the most of the time (the largest probability) at large separations. The dissociation occurs if the energy of relative $\text{O}_2 + \text{O}$ rotation is transferred into

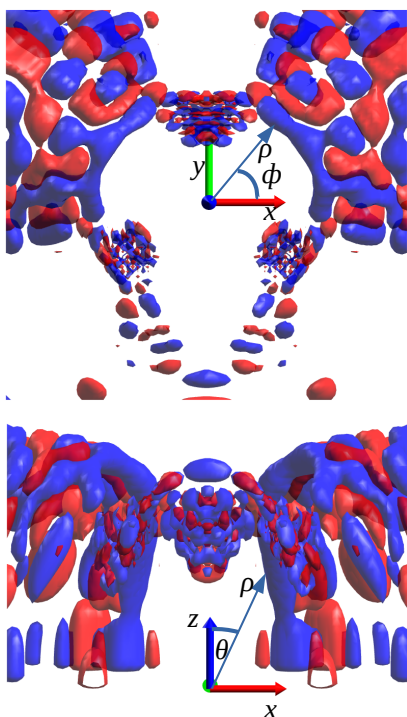


FIG. 15: The resonance with $E = 8599.12 \text{ cm}^{-1}$, $\tau = 3.3 \text{ ps}$, corresponding to rotational roaming of the ^{18}O oxygen around the light diatomic fragment $^{16}\text{O}^{16}\text{O}$. The wave function is shown for the isosurface value 0.01. Compare it with Fig. 5, showing a similar state at a fixed value of ρ , approaching the dissociative region. Here the wave function is shown in the three dimensions, for a fixed isosurface value, showing multiple nodes in all three dimensions. The resonance is mainly localized in the valley at $\rho > 6$, corresponding to the lower part of Fig. 5. This clearly indicates the decay character of the resonance.

relative vibrational motion of the fragments, i.e. to the dissociative coordinate. Therefore, such resonances could be referred as rotational roaming resonances. They are similar in character to shape resonances in electron-atom or electron-molecule collisions, meaning that they could be viewed as if the resonant part of their wave function is bound by a centrifugal barrier due to the relative rotational motion. Another example rotational roaming resonance is shown in Fig. 15.

The rotational roaming resonances decay relatively quickly, having lifetimes of the order of a picosecond or less. This is similar to relatively short lifetimes of shape resonances in electron-atom or electron-molecule collisions.

D. Rovibrational roaming

The rotating O_2 molecule in the rotational roaming type of resonances can also be excited vibrationally, as demonstrated by the wave function shown in Figs. 6 and 7. In this situation, the O_2 and O fragments also stay at large distances. Such resonances decay by the energy transfer from the O_2 rovibrational motion to the $\text{O}_2 + \text{O}$ dissociative degree of freedom. Such resonances could be referred as rovibrational roaming Feshbach resonances. They have very long lifetimes, approaching 100 ps.

E. Delocalised resonances

The largest class of resonances are different combinations of the above types. Figure 16 shows an example of such a resonance. The upper panel of the figure, showing the amplitude of a larger value, demonstrates that the wave function is not negligible in the regions of the three potential wells and also in the $^{16}\text{O} + ^{16}\text{O}^{18}\text{O}$ and $^{16}\text{O} + ^{18}\text{O}^{16}\text{O}$ valley regions, where it has a character of the rotational roaming state, while the wave function is not visible in the $^{18}\text{O} + ^{16}\text{O}_2$ valley. The smaller amplitude figure (the lower panel) demonstrates that in the $^{18}\text{O} + ^{16}\text{O}_2$ valley the wave function is not completely negligible and corresponds generally to rotationless motion, with no nodes along ϕ in the $^{18}\text{O} + ^{16}\text{O}_2$ dissociative channel.

VI. CONCLUSION

Energies and lifetimes of vibrational resonances were computed for the ^{18}O -enriched isotopologue $^{50}\text{O}_3 = \{^{16}\text{O}^{16}\text{O}^{18}\text{O} \text{ and } ^{16}\text{O}^{18}\text{O}^{16}\text{O}\}$ of the ozone molecule using hyperspherical coordinates and the method of complex absorbing potential. Various types of the scattering resonances were identified, including roaming $\text{OO}-\text{O}$ rotational states and the series corresponding to continuation of bound vibrational resonances of highly excited bending or symmetric stretching vibrational modes. Such series become metastable above the dissociation limit. Different paths for the formation decay of symmetric $^{16}\text{O}^{18}\text{O}^{16}\text{O}$ and asymmetric species $^{16}\text{O}^{16}\text{O}^{18}\text{O}$ were also identified.

Previous theoretical studies [69–71] of the $^{16}\text{O}^{16}\text{O}^{18}\text{O}$ system, devoted to the isotope-exchange reaction $^{16}\text{O}_2 + ^{18}\text{O} \rightarrow ^{16}\text{O}^{18}\text{O} + ^{16}\text{O}$, with the same *ab initio* PES provided a good agreement with experimental observations [64, 120] (and references therein). It was found that topographic characteristics of the full-dimensional PES shape in the neighborhood of the transition states region results in a dramatic effect in the kinetic rate constant of the reaction, which is an intermediate step of the isotopic formation of reaction (1). Also, the recent classical trajectory calculations [40] for the formation of ozone in

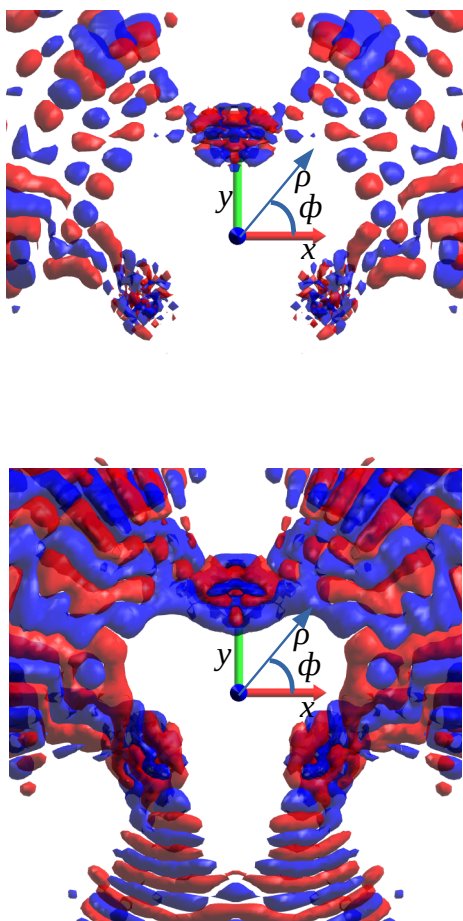


FIG. 16: An example of a resonance delocalised between the three potential wells with $E = 8757 \text{ cm}^{-1}$ and lifetime $\tau = 2.3 \text{ ps}$. The wave function is shown for isosurface values 0.01 (upper panel) and 0.003 (lower panel).

ternary collisions were able to reproduce several experimental observations.

Obtained energies and lifetimes of the vibrational resonances confirms the existence of many resonances in the 66+8 and 68+6 roaming channels (Fig. 10) having lifetimes of 0.3-0.5 ps, which is a typical time scale of the isotope-exchange process as was determined by the wave packet propagation method in [71] using the same PES. On the other hand, there appear long-lived resonances with lifetimes longer by two or three orders of magnitude (Figs. 10 and 11). Such lifetimes are needed for the stabilisation process in ternary collisions.

The energies and lifetimes of the vibrational resonances computed in this work are provided in the supplementary material. This information could be useful in future works to study the formation of $^{16}\text{O}^{18}\text{O}^{16}\text{O}$ and $^{16}\text{O}^{16}\text{O}^{18}\text{O}$ in ternary collisions, involving a diatomic oxygen, an oxygen atom, and a third particle (Ar or N_2 , for example). Densities and lifetimes of resonances leading to the $^{16}\text{O}_2 + ^{18}\text{O}$ dissociation channel and to the $^{16}\text{O}^{18}\text{O} + ^{16}\text{O}$ channel, are different. Combined with the results of our previous calculations of resonances in the $^{16}\text{O}_3$ molecule and obtained densities and lifetimes in the only one channel $^{16}\text{O}_2 + ^{16}\text{O}$, our preliminary calculations suggest that there is a significant difference in the rate of formation of $^{16}\text{O}_3$ and $^{16}\text{O}^{16}\text{O}^{18}\text{O}$ $^{16}\text{O}^{18}\text{O}^{16}\text{O}$ in ternary collisions.

Though the MIF issue has not yet been solved in terms of the complete theoretical first-principle modelling, the analysis of various possible types of scattering resonances and values of their lifetimes computed in this work could pave the way to a further progress in the understanding of the background dynamics of this challenging problem.

Acknowledgements This work was supported by the RSF project no. 19-12-00171-P for the ozone analyses and the National Science Foundation, Grant No.2110279 for the method of calculations.

-
- [1] C. A. Brenninkmeijer, C. Janssen, J. Kaiser, T. Röckmann, T. Rhee and S. Assonov, *Chem. Rev.*, 2003, **103**, 5125–5162.
- [2] B. Luz and E. Barkan, *Geochim. Cosmochim. Acta*, 2005, **69**, 1099–1110.
- [3] J. M. Eiler, *Annu. Rev. Earth Planet. Sci.*, 2013, **41**, 411–441.
- [4] N. Dauphas and E. A. Schauble, *Annu. Rev. Earth Planet. Sci.*, 2016, **44**, 709–783.
- [5] M. H. Thiemens and M. Lin, *Angewandte Chemie*, 2019, **131**, 6898–6916.
- [6] J. M. Carlstad and K. A. Boering, *Annu. Rev. Phys. Chem.*, 2023, **74**, 439–465.
- [7] N. Prantzos, O. Aubert and J. Audouze, *Astronomy and Astrophysics*, v. 309, p. 760-774, 1996, **309**, 760–774.
- [8] C. M. Alexander and L. R. Nittler, *Astrophys. J.*, 1999, **519**, 222.
- [9] M. Gounelle and A. Meibom, *Astrophys. J.*, 2007, **664**, L123.
- [10] E. D. Young, K. Kuramoto, R. A. Marcus, H. Yurimoto and S. B. Jacobsen, *Rev. Mineral. Geochem.*, 2008, **68**, 187–218.
- [11] R. Smith, M. Gai, S. Stern, D. Schweitzer and M. Ahmed, *Nat. Commun.*, 2021, **12**, 5920.
- [12] T. R. Ireland, J. Avila, R. C. Greenwood, L. J. Hicks and J. C. Bridges, *Space Science Reviews*, 2020, **216**, 25.
- [13] R. N. Clayton, *Annu. Rev. Earth Planet. Sci.*, 1993, **21**, 115–149.
- [14] E. D. Young, A. Galy and H. Nagahara, *Geochim. Cosmochim. Acta*, 2002, **66**, 1095–1104.
- [15] H. Wiesemeyer, R. Güsten, R. Aladro, B. Klein, H.-W. Hübers, H. Richter, U. U. Graf, M. Justen, Y. Okada and J. Stutzki, *Phys. Rev. Res.*, 2023, **5**, 013072.
- [16] L. Y. Yeung, J. L. Ash and E. D. Young, *Science*, 2015, **348**, 431–434.

- [17] P. Alexandre, *Isotopes and the natural environment*, Springer Nature, 2020.
- [18] R. E. Weston Jr, *Chem. Rev.*, 1999, **99**, 2115.
- [19] M. H. Thiemens, *Annu. Rev. Earth Planet. Sci.*, 2006, **34**, 217–262.
- [20] M. H. Thiemens, S. Chakraborty and G. Dominguez, *Annu. Rev. Phys. Chem.*, 2012, **63**, 155–177.
- [21] M. Brinjikji and J. R. Lyons, *Rev. Mineral. Geochem.*, 2021, **86**, 197–216.
- [22] K. Mauersberger, *Geophys. Res. Lett.*, 1981, **8**, 935–937.
- [23] M. H. Thiemens and J. E. Heidenreich III, *Science*, 1983, **219**, 1073–1075.
- [24] J. E. Heidenreich III and M. H. Thiemens, *J. Chem. Phys.*, 1986, **84**, 2129–2136.
- [25] D. Krankowsky and K. Mauersberger, *Science*, 1996, **274**, 1324–1325.
- [26] K. Mauersberger, B. Erbacher, D. Krankowsky, J. Gunther and R. Nickel, *Science*, 1999, **283**, 370–372.
- [27] K. Mauersberger, D. Krankowsky, C. Janssen and R. Schinke, *Adv. At., Mol., Opt. Phys.*, Elsevier, 2005, vol. 50, pp. 1–54.
- [28] Y. Q. Gao and R. Marcus, *Science*, 2001, **293**, 259–263.
- [29] C. Janssen, J. Guenther, D. Krankowsky and K. Mauersberger, *Chem. Phys. Lett.*, 2003, **367**, 34–38.
- [30] R. Schinke, S. Y. Grebenshchikov, M. Ivanov and P. Fleurat-Lessard, *Annu. Rev. Phys. Chem.*, 2006, **57**, 625–661.
- [31] R. A. Marcus, *Proc. Nat. Ac. Scien.*, 2013, **110**, 17703–17707.
- [32] K. Feilberg, A. Wiegel and K. Boering, *Chem. Phys. Lett.*, 2013, **556**, 1–8.
- [33] D. Krankowsky, P. Lämmerzahl and K. Mauersberger, *Geophys. Res. Lett.*, 2000, **27**, 2593–2595.
- [34] R. Dawes, P. Lolur, J. Ma and H. Guo, *J. Chem. Phys.*, 2011, **135**, 081102.
- [35] J. Guenther, B. Erbacher, D. Krankowsky and K. Mauersberger, *Chem. Phys. Lett.*, 1999, **306**, 209–213.
- [36] K. Mauersberger, D. Krankowsky and C. Janssen, Solar System History from Isotopic Signatures of Volatile Elements: Volume Resulting from an ISSI Workshop 14–18 January 2002, Bern, Switzerland, 2003, pp. 265–279.
- [37] C. Janssen, *PhD thesis*, Ruprecht-Karls-Universität Heidelberg, 2004.
- [38] C. Janssen, *J. Geophys. Res. Atmos.*, 2005, **110**, year.
- [39] K. Luther, K. Oum and J. Troe, *Phys. Chem. Chem. Phys.*, 2005, **7**, 2764–2770.
- [40] M. Mirahmadi, J. Pérez-Ríos, O. Egorov, V. Tyuterev and V. Kokoouline, *Phys. Rev. Lett.*, 2022, **128**, 108501.
- [41] C. Janssen, J. Guenther, D. Krankowsky and K. Mauersberger, *J. Chem. Phys.*, 1999, **111**, 7179–7182.
- [42] B. Hathorn and R. Marcus, *J. Chem. Phys.*, 2000, **113**, 9497–9509.
- [43] Y. Q. Gao and R. Marcus, *J. Chem. Phys.*, 2002, **116**, 137–154.
- [44] Y. Q. Gao and R. Marcus, *J. Chem. Phys.*, 2007, **127**, year.
- [45] C. Janssen and R. Marcus, *Science*, 2001, **294**, 951–951.
- [46] R. Schinke, P. Fleurat-Lessard and S. Y. Grebenshchikov, *Phys. Chem. Chem. Phys.*, 2003, **5**, 1966–1969.
- [47] P. Reinhardt and F. Robert, *Earth Planet. Sci. Lett.*, 2013, **368**, 195–203.
- [48] A. Teplukhin and D. Babikov, *Faraday Discuss.*, 2018, **212**, 259–280.
- [49] F. Holka, P. G. Szalay, T. Müller and V. G. Tyuterev, *J. Phys. Chem. A*, 2010, **114**, 9927–9935.
- [50] V. G. Tyuterev, R. V. Kochanov, S. A. Tashkun, F. Holka and P. G. Szalay, *J. Chem. Phys.*, 2013, **139**, 134307.
- [51] R. Dawes, P. Lolur, A. Li, B. Jiang and H. Guo, *J. Chem. Phys.*, 2013, **139**, 201103.
- [52] A. Tajti, P. G. Szalay, R. Kochanov and V. G. Tyuterev, *Phys. Chem. Chem. Phys.*, 2020, **22**, 24257–24269.
- [53] V. G. Tyuterev, R. V. Kochanov and S. A. Tashkun, *J. Chem. Phys.*, 2017, **146**, 064304.
- [54] D. Lapierre, A. Alijah, R. Kochanov, V. Kokoouline and V. Tyuterev, *Phys. Rev. A*, 2016, **94**, 042514.
- [55] S. Ndengué, R. Dawes, X.-G. Wang, T. Carrington Jr, Z. Sun and H. Guo, *J. Chem. Phys.*, 2016, **144**, 074302.
- [56] A. Teplukhin and D. Babikov, *J. Chem. Phys.*, 2016, **145**, 114106.
- [57] V. Kokoouline, D. Lapierre, A. Alijah and V. Tyuterev, *Phys. Chem. Chem. Phys.*, 2020, **22**, 15885–15899.
- [58] A. Campargue, S. Kassi, D. Romanini, A. Barbe, M.-R. De Backer-Barilly and V. G. Tyuterev, *J. Mol. Spectrosc.*, 2006, **240**, 1–13.
- [59] D. Mondelain, A. Campargue, S. Kassi, A. Barbe, E. Starikova, M.-R. De Backer and V. G. Tyuterev, *J. Quant. Spectrosc. Radiat. Transfer*, 2013, **116**, 49–66.
- [60] S. Vasilchenko, A. Barbe, E. Starikova, S. Kassi, D. Mondelain, A. Campargue and V. Tyuterev, *Phys. Rev. A*, 2020, **102**, 052804.
- [61] S. Vasilchenko, A. Barbe, E. Starikova, S. Kassi, D. Mondelain, A. Campargue and V. Tyuterev, *J. Quant. Spectrosc. Radiat. Transfer*, 2022, **278**, 108017.
- [62] M. R. Wiegell, N. W. Larsen, T. Pedersen and H. Egsgaard, *Int. J. Chem. Kinet.*, 1997, **29**, 745–753.
- [63] M. Anderson, J. Ensher, M. Matthews, C. Wieman and E. Cornell, *Science*, 1995, **269**, 198–201.
- [64] P. Fleurat-Lessard, S. Y. Grebenshchikov, R. Siebert, R. Schinke and N. Halberstadt, *J. Chem. Phys.*, 2003, **118**, 610–621.
- [65] Y. Li, Z. Sun, B. Jiang, D. Xie, R. Dawes and H. Guo, *J. Chem. Phys.*, 2014, **141**, 081102.
- [66] Z. Sun, D. Yu, W. Xie, J. Hou, R. Dawes and H. Guo, *J. Chem. Phys.*, 2015, **142**, 174312.
- [67] G. Guillon, T. R. Rao, S. Mahapatra and P. Honvault, *J. Phys. Chem. A*, 2015, **119**, 12512–12516.
- [68] S. A. Lahankar, J. Zhang, T. K. Minton, H. Guo and G. Lendvay, *J. Phys. Chem. A*, 2016, **120**, 5348–5359.
- [69] G. Guillon, P. Honvault, R. Kochanov and V. Tyuterev, *The Journal of Physical Chemistry Letters*, 2018, **9**, 1931–1936.
- [70] P. Honvault, G. Guillon, R. Kochanov and V. Tyuterev, *J. Chem. Phys.*, 2018, **149**, 214304.
- [71] C. H. Yuen, D. Lapierre, F. Gatti, V. Kokoouline and V. G. Tyuterev, *J. Phys. Chem. A*, 2019, **123**, 7733–7743.
- [72] Z. Sun, L. Liu, S. Y. Lin, R. Schinke, H. Guo and D. H. Zhang, *Proc. Nat. Ac. Scien.*, 2010, **107**, 555–558.
- [73] A. L. Van Wyngarden, K. A. Mar, J. Quach, A. P. Nguyen, A. A. Wiegel, S.-Y. Lin, G. Lendvay, H. Guo, J. J. Lin, Y. T. Lee *et al.*, *J. Chem. Phys.*, 2014, **141**, year.
- [74] S. A. Ndengué, R. Schinke, F. Gatti, H.-D. Meyer and R. Jost, *J. Phys. Chem. A*, 2012, **116**, 12271–12279.

- [75] S. Ndengué, S. Madronich, F. Gatti, H.-D. Meyer, O. Motapon and R. Jost, *J. Geophys. Res. Atmos.*, 2014, **119**, 4286–4302.
- [76] S. Sur, S. A. Ndengué, E. Quintas-Sánchez, C. Bop, F. Lique and R. Dawes, *Phys. Chem. Chem. Phys.*, 2020, **22**, 1869–1880.
- [77] P. García-Fernandez, I. B. Bersuker and J. E. Boggs, *Phys. Rev. Lett.*, 2006, **96**, 163005.
- [78] A. Alijah, D. Lapierre and V. Tyuterev, *Mol. Phys.*, 2018, **116**, 2660–2670.
- [79] R. Schinke and P. Fleurat-Lessard, *J. Chem. Phys.*, 2005, **122**, year.
- [80] M. V. Ivanov, S. Y. Grebenshchikov and R. Schinke, *J. Chem. Phys.*, 2009, **130**, year.
- [81] D. Babikov, B. Kendrick, R. Walker, R. Schinke and R. Pack, *Chem Phys Lett*, 2003, **372**, 686–691.
- [82] A. Teplukhin, I. Gayday and D. Babikov, *J. Chem. Phys.*, 2018, **149**, year.
- [83] I. Gayday, A. Teplukhin and D. Babikov, *J. Chem. Phys.*, 2019, **150**, 101104.
- [84] I. Gayday, A. Teplukhin, B. K. Kendrick and D. Babikov, *J. Chem. Phys.*, 2020, **152**, 144104.
- [85] D. Babikov, E. Grushnikova, I. Gayday and A. Teplukhin, *Molecules*, 2021, **26**, 1289.
- [86] D. Charlo and D. C. Clary, *J. Chem. Phys.*, 2002, **117**, 1660–1672.
- [87] T. Xie and J. M. Bowman, *Chem. Phys. Lett.*, 2005, **412**, 131–134.
- [88] M. Kryvohuz and R. Marcus, *J. Chem. Phys.*, 2010, **132**, year.
- [89] P. Reinhardt and F. Robert, *Chem. Phys.*, 2018, **513**, 287–294.
- [90] F. Robert, L. Baraut-Guinet, P. Cartigny and P. Reinhardt, *Chem. Phys.*, 2019, **523**, 191–197.
- [91] N. Sakamoto, Y. Seto, S. Itoh, K. Kuramoto, K. Fujino, K. Nagashima, A. N. Krot and H. Yurimoto, *Science*, 2007, **317**, 231–233.
- [92] L. Y. Yeung, L. T. Murray, A. Banerjee, X. Tie, Y. Yan, E. L. Atlas, S. M. Schauffler and K. A. Boering, *J. Geophys. Res. Atmos.*, 2021, **126**, e2021JD034770.
- [93] S. Gromov and C. Brenninkmeijer, *Atmos. Chem. Phys.*, 2015, **15**, 1901–1912.
- [94] B. Jonkheid, T. Röckmann, N. Glatthor, C. Janssen, G. Stiller and T. Von Clarmann, *Atmos. Meas. Tech.*, 2016, **9**, 6069–6079.
- [95] C.-H. Huang, S. Bhattacharya, Z.-M. Hsieh, Y.-J. Chen, T.-S. Yih and M.-C. Liang, *Earth Space Sci.*, 2019, **6**, 752–773.
- [96] L. Y. Yeung, L. T. Murray, P. Martinerie, E. Witrant, H. Hu, A. Banerjee, A. Orsi and J. Chappellaz, *Nature*, 2019, **570**, 224–227.
- [97] M. Evans, *nature*, 2019, **570**, 167–168.
- [98] C. Janssen and B. Tuzson, *J. Phys. Chem. A*, 2010, **114**, 9709–9719.
- [99] F. Robert and P. Reinhardt, *Chem. Phys. Impact*, 2022, **4**, 100073.
- [100] M. Sierra-Olea, S. Kölle, E. Bein, T. Reemtsma, O. J. Lechtenfeld and U. Hübner, *Water Res.*, 2023, **233**, 119740.
- [101] V. G. Tyuterev, R. Kochanov, A. Campargue, S. Kassi, D. Mondelain, A. Barbe, E. Starikova, M. R. De Backer, P. G. Szalay and S. Tashkun, *Phys. Rev. Lett.*, 2014, **113**, 143002.
- [102] A. Barbe, S. Mikhailenko, E. Starikova and V. Tyuterev, *Molecules*, 2022, **27**, 911.
- [103] D. J. Tannor, *J. Am. Chem. Soc.*, 1989, **111**, 2772–2776.
- [104] B. R. Johnson, *J. Chem. Phys.*, 1983, **79**, 1916.
- [105] V. Kokoouline and F. Masnou-Seeuws, *Phys. Rev. A*, 2006, **73**, 012702.
- [106] J. Blandon, V. Kokoouline and F. Masnou-Seeuws, *Phys. Rev. A*, 2007, **75**, 042508.
- [107] J. Blandon and V. Kokoouline, *Phys. Rev. Lett.*, 2009, **102**, 143002.
- [108] A. Alijah, *J. Mol. Spectrosc.*, 2010, **264**, 111–119.
- [109] A. Alijah and V. Kokoouline, *Chem. Phys.*, 2015, **460**, 43.
- [110] D. Townsend, S. A. Lahankar, S. K. Lee, S. D. Chembreau, A. G. Suits, X. Zhang, J. Rheinecker, L. Harding and J. M. Bowman, *Science*, 2004, **306**, 1158–1161.
- [111] A. G. Suits, *Acc. Chem. Res.*, 2008, **41**, 873–881.
- [112] J. M. Bowman, *Mol. Phys.*, 2014, **112**, 2516–2528.
- [113] F. A. Mauguère, P. Collins, Z. C. Kramer, B. K. Carpenter, G. S. Ezra, S. C. Farantos and S. Wiggins, *J. Chem. Phys.*, 2016, **144**, year.
- [114] R. C. Whitten and F. T. Smith, *J. Math. Phys.*, 1968, **9**, 1103.
- [115] O. I. Tolstikhin, S. Watanabe and M. Matsuzawa, *J. Phys. B: At. Mol. Opt. Phys.*, 1996, **29**, L389.
- [116] I. Tuvi and Y. B. Band, *J. Chem. Phys.*, 1997, **107**, 9079–9084.
- [117] V. Kokoouline, O. Dulieu, R. Kosloff and F. Masnou-Seeuws, *J. Chem. Phys.*, 1999, **110**, 9865.
- [118] N. Douguet, J. Blandon and V. Kokoouline, *J. Phys. B: At. Mol. Opt. Phys.*, 2008, **41**, 045202.
- [119] A. M. Arthurs and A. Dalgarno, *Proc. Math. Phys. Eng. Sci. P Roy. Soc. A-Math. Phys.*, 1960, **256**, 540–551.
- [120] S. Anderson, D. Hülsebusch and K. Mauersberger, *J. Chem. Phys.*, 1997, **107**, 5385–5392.
- [121] P. R. Bunker and P. Jensen, *Molecular Symmetry and Spectroscopy*, NRC Research Press, 1998.
- [122] This choice is different from that of Bunker & Jensen [121]. As a result, the symmetry labels B_1 and B_2 are interchanged.